Revue des Composites et des Matériaux Avancés-Journal of Composite and Advanced Materials
Vol. 36, No. 2, April, 2026, pp. 335-347
Journal homepage: http://iieta.org/journals/rcma

Photocatalytic Performance of PAN-PMMA Hybrid Nanofibers Reinforced with Hydrothermally Synthesized CeO₂ Nanoparticles

Mohammed A. Kadhim, Fouad Sh. Hashim, Shurooq S. Abed Al-Abbas*

Department of Physics, College of Education for Pure Sciences, University of Babylon, Babylon 51001, Iraq

Corresponding Author Email: alsaadimohammed611@gmail.com

https://doi.org/10.18280/rcma.360210

Received: 18 February 2026
Revised: 20 March 2026
Accepted: 3 April 2026
Available online: 30 April 2026

Keywords:
PAN-PMMA hybrid fibers, CeO₂ nanoparticles, hydrothermal synthesis, synergistic photocatalytic activity, polymer nanocomposite fibers, electrospinning

ABSTRACT

In this research, CeO_2 nanoparticles were synthesized by the hydrothermal route, with the pH maintained at 9, resulting in an average particle size of 81.35 ± 12.48 nm, as determined by ImageJ analysis of 100 measurements. Afterward, polyacrylonitrile (PAN) and poly (methyl methacrylate) (PMMA) blends/CeO_2 nanocomposite fiber mats were produced by electrospinning to degrade dyes in the presence of ultraviolet (UV) light. Characterization of the samples was performed using X-ray diffraction (XRD), Fourier transform infrared spectroscopy (FTIR), field emission scanning electron microscope (FE-SEM), energy dispersive X-ray spectroscopy (EDX), and ultraviolet-visible (UV-Vis) spectroscopy. The XRD data proved the crystallinity of CeO_2 with a cubic structure, while FTIR spectra exhibited intense interactions among PAN, PMMA, and CeO_2 nanomaterials. FE-SEM micrographs showed that the fibers were uniformly distributed and interconnected, and EDX analysis confirmed the presence of CeO_2 in the polymer matrix. The optical energy gap decreased from 3.4 eV to 2.6 eV upon CeO_2 loading, suggesting improved optical properties. Furthermore, the average fiber diameter also reduced from 131.12 ± 21.9 nm at 0.0 wt.% CeO_2 to 107.3 ± 14.56 nm at 6.6 wt.% CeO_2 based on ImageJ calculation from 100 measurements, which may be linked to improved solution conductivity and better jet stretching behavior during electrospinning. As shown in the photocatalytic studies, about 80% of methylene blue (M.B.) was decomposed within an hour under UV irradiation, demonstrating effective photocatalytic activity. The decomposition was found to be strongly time-dependent. According to kinetic studies, the rate of decomposition is described by a first-order model with a rate constant $k = 0.0253\ min^{-1}$ and an R^2 value of 0.99. This increase in photocatalytic activity is due to charge separation, reduced electron recombination, and the potential role of CeO_2 assisting in electron transfer within the PAN-PMMA matrix. These results suggest how this material can be used for photocatalytic purposes. Further research should focus on the reusability and stability of the nanofibers produced.

1. INTRODUCTION

Water pollution and environmental pollution, particularly noticeable in the context of climate change, are among the most pressing issues today [1]. This problem affects not just humans but also human health [2] and quality of life [3]. Untreated industrial effluent is among the most significant sources of environmental pollution [4]. Its direct discharge into surface waters leads to serious freshwater pollution [5]. Therefore, the removal of these organic pollutants is among the most urgent environmental challenges of the 21st century [6, 7]. Over the past two decades, demand for effective methods to remove these pollutants has increased. Photocatalysis is one of the most important of these methods, offering a new and attractive approach to using ultraviolet-visible (UV-Vis) spectroscopy to generate catalysts that induce oxidation/reduction reactions, thus breaking down these pollutants [8]. The performance of traditional catalysts faces some challenges, such as limited spectral recombination of the resulting holes and electrons due to visible-light absorption, and difficulties in repeatedly reusing the catalyst. It has led to an increased need for stable, effective materials that mitigate these difficulties and can be used as photocatalysts or photovoltaic agents in wastewater treatment utilising UV or visible-light irradiation. In recent years, a strategy has emerged to incorporate optically active metal oxides into polymer matrices as nanofibers, typically prepared via electrospinning [9]. Electrospinning is the most efficient method for producing nanometer-diameter stranded fibers. Thanks to its excellent fibrous structure, electrospinning produces a highly porous polymer film with good mechanical strength [10]. The nanofibers are produced by applying an electric current to a polymer mixture. On a grounded collector, the spun nanofibers are gathered as a non-woven mat [11]. The properties of the spun nanofibers can be improved by selecting appropriate raw materials (polymers), suitable solvents, and production processes, and by optimizing processing conditions. The physical characteristics of the synthesised nanofibers are primarily ascribed to their morphology, diameter, and specific surface area [12]. The curing process, the concentration of the raw material solution, the type of solvent, and adjustments to the electrospinning parameters, including the applied voltage, solution flow rate, and the distance between the needle and collector, among others [13].

This study focused on the use of PAN-PMMA due to its thermal stability and the use of CeO_2 nanoparticles [14] and cytes [15]. Their low cost and ease of availability are key advantages. PAN's main properties include its ability to dissolve ions, its thermal and electrochemical stability, its ease of processing, and its resistance to oxidative degradation [16]. Because PMMA works well with liquid electrolytes, it has high transparency and a strong electrolyte-absorption capacity [17]. Thus, desired features are obtained when PAN and PMMA are combined in a single membrane [18]. The electrochemical and electrospinning characteristics of these two polymers have been reported separately by several researchers [19]. It has recently been suggested that suitable properties for this amalgamation, characterised by consistent dimensions and clearly delineated form, can be achieved using the electrospinning method [20]. Metal oxide semiconductors (MOS) have received considerable attention. Among these materials, CeO_2 is one of the most widely used semiconductors as a photocatalyst and photoelectric catalyst in various pollutant treatment processes [21]. Several techniques, such as pH modification [22], doping with metallic and non-metallic ions, crosslinking with other semiconductors, and incorporating CeO_2 into supporting polymers, can increase its photocatalytic and photoelectric activity in wastewater treatment [23]. The primary characteristics of CeO_2 that make it a valuable material for photocatalysis are its strong band gap and elevated optical clarity in the visible spectrum [24]. Significant oxygen storage capacity, remarkable chemical reactivity, and high refractive index, all of which are utilized in the degradation of different contaminants [25]. It should be noted that CeO_2 has excellent toughness and thermal stability, excellent conductivity of oxygen ions, distinctive redox characteristics, and easy conversion between the oxidation states Ce (IV) and Ce (III) [26]. As a result, the aforementioned characteristics show that CeO_2 may be used practically as a photocatalyst or photoelectric in wastewater treatment [27], as well as in a variety of other practical applications, like coating metals and alloys to prevent rust and corrosion [28]. The PAN-PMMA/CeO_2 structure has not yet been studied; therefore, in this research, PAN-PMMA/CeO_2 nanocomposite fibers (NCFs) were electrospun. The incorporation of CeO_2 into polymer fibers such as PAN or PMMA or their combination provides several practical advantages, such as stabilizing CeO_2 molecules on the surface of a flexible and easy-to-handle matrix, increasing the surface area available for reaction, and improving charge separation through the formation of nano-interfaces/structures, etc. They may be used in important applications such as photocatalysis and antibacterial agents.

2. EXPERIMENTAL DETAILS

2.1 Materials

The following chemicals were used as received without further purification: Cerium precursors $(NH_4)_2[Ce(NO_3)_6]$ (99.0%, Mw = 548.23 g/mol) was obtained from LOBA Chemie (Mumbai, India). Sodium hydroxide (NaOH, 99.0%, Mw = 40 g/mol) and hydrochloric acid (HCl, 35-38%, Mw = 36.46 g/mol) were purchased from Himedia (Mumbai, India) and Thomas Baker (India), respectively. Throughout each experiment, ultra-pure water and ethanol were used. Polyacrylonitrile (PAN) powder (150,000 g/mol, purity ≥ 99%) was acquired from Sigma-Aldrich (Merck KGaA, Darmstadt, Germany). Poly(methyl methacrylate) (PMMA) granules (Mw = 20000 g/mol, purity ≥ 99%) were purchased from Thomas Baker Laboratory Reagent Co, Ltd, India, and the organic amide solvent N, N-dimethylformamide (DMF) (Mw = 73.09 g/mol, purity ≥ 99.7%) was purchased from Alpha Chemika (Mumbai, India). All solvents were used as is.

2.2 Fabrication of CeO_2 nanoparticles using the hydrothermal methodology

To prepare the sodium hydroxide solution (NaOH), 2.62 g (powder) in 110 mL deionized water was prepared, and 6 g of cerium ammonium nitrate (Ce $(NH_4)_2(NO_3)_6$) was dissolved in 55 mL deionized water while continuously stirring for 15 minutes until all the materials were completely dissolved. The prepared NaOH solution was added to the cerium solution by dripping while stirring, and the mixture was stirred for an additional 30 minutes to form a uniform mixture. After that, the solution was titrated with HCl, 35-38% Thomas Baker, dropwise under stirring, using a calibrated Jenway 3540 pH/Conductivity Meter to maintain a pH of 9. After that, the solution was placed in an autoclave for hydrothermal synthesis at 180 °C for 5 hours.

Upon naturally cooling the system to ambient temperature, the product was isolated from the mother liquor by centrifugation at 4000 rpm, washed three times with ethanol and three times with deionized water to remove any residual material, and finally dried at 50-70 °C for 3 hours. The formed powder was annealed using a two-stage annealing procedure (performed only on the formed nanoparticles before incorporating them into polymers) to confirm their phase purity and enhanced crystallinity. The powder was annealed at 250 °C for 2.5 hours to eliminate any impurity, and subsequently annealed again at 500 °C for 2.5 hours for the crystallization of CeO_2. Annealing was performed using a furnace-cooling method to reduce thermal-shock-induced defect formation. Lastly, the annealed sample was milled to yield CeO_2 nanoparticles, as depicted in Figure 1.

2.3 Preparations of PAN-PMMA/CeO_2 nanocomposite fibers

To begin with, 0.85 g of PAN was slowly dissolved in 8 mL of DMF using continuous stirring for 6 h at room temperature. Later, 0.15 g of PMMA was added to the system, and stirring was continued for another 6 h to prepare a homogeneous polymer blend. Then, the obtained PAN-PMMA blend was mixed with CeO_2 nanoparticles with various contents (2.2, 4.4, and 6.6 wt.%) relative to the total weight of the polymer blend (PAN + PMMA). Accordingly, the mass of the polymer blend was reduced to 0.978, 0.956, and 0.934 g, respectively. After that, the mixtures were stirred for 50 min at room temperature and sonicated for 3 min to attain a uniformly dispersed solution. The exact composition of electrospinning solutions is shown in Table 1. The prepared solutions were used to electrospin PAN-PMMA/CeO_2 NCFs.

Table 1. Preparation of PAN-PMMA/CeO_2 nanofiber precursor solutions

Sample	PAN (g)	PMMA (g)	CeO2 (g)	DMF (ml)
S_0	0.85	0.15	0.0	8
S_1	0.8313	0.1467	0.022	8
S_2	0.8126	0.1434	0.044	8
S_3	0.7939	0.1401	0.066	8

2.4 Fabrication of PAN-PMMA/CeO_2 nanocomposite fibers

The drum collector was covered with aluminum foil, while glass substrates (7.5 × 2.5 cm^2) were attached to the collector using adhesive tape for optical characterization. A 3 mL syringe with a 1.2 mm inner diameter needle was used in dispensing the PAN-PMMA solutions as well as PAN-PMMA solutions with different amounts of CeO_2 (0.0, 2.2, 4.4, and 6.6 wt.%). High voltage (8.5 kV) was applied to the needle, while the collector spun at 300 rpm. Experiments were performed under ambient conditions (25 ± 2 °C, approximately 40-60% relative humidity). The flow rate was kept constant at 0.3 mL h^{-1}, and electrospinning was performed for 2 hours. The distance from the needle tip to the collector was kept constant at 7 cm to ensure stable jet formation during electrospinning, as shown in Figure 1.

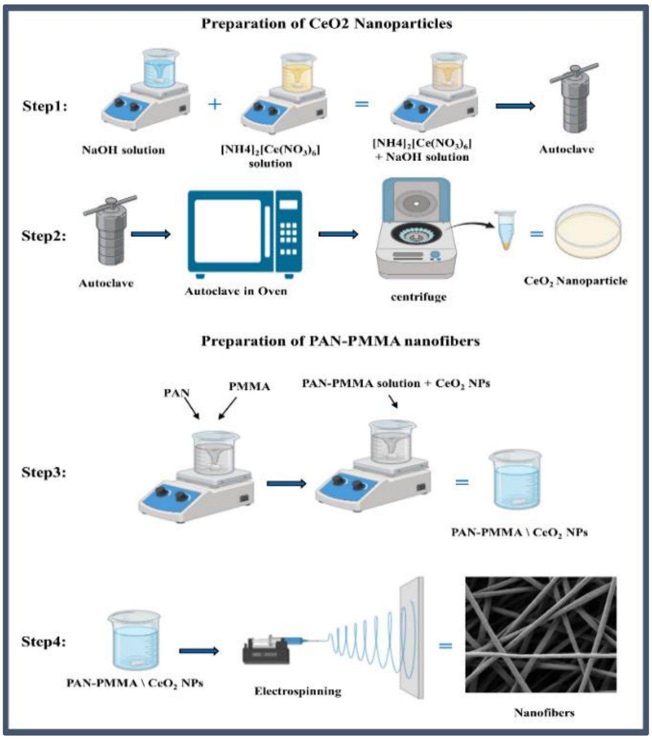

Figure 1. Stages of synthesis of CeO_2 nanoparticles and PAN-PMMA/CeO_2 fibers

Note: PAN = polyacrylonitrile, PMMA= poly (methyl methacrylate)

2.5 Photocatalytic decomposition experiment

Methylene blue (M.B.) degradation in aqueous media was used to assess the photocatalytic activity of the PAN-PMMA/CeO_2 NCFs. 0.08 mg of dye was dissolved in 70 mL of deionized water to form a solution, which was then agitated for 30 minutes to ensure consistency. To determine the starting concentration (A_0), a sample was first collected for photoabsorption analysis. The solution was then supplemented with 0.5 g of electrospun NCFs. To achieve a balance between adsorption and absorption at the nanofiber surface, the mixture was incubated in complete darkness for 15 minutes. After that, the dye-fiber mixture was exposed to UV light in the 320-400 nm range at a distance of 8 cm and a radiative intensity of 3.8 mW/cm^2, with a total power of 112 W (14 × 8 W) (Figure 2). The solution was then extracted in 5-milliliter aliquots at 15-minute intervals. Centrifugation was used to separate the precipitate from the catalyst. UV-Vis spectroscopy was then used to analyse the samples' absorbance and to calculate changes in concentration (A_t) over time.

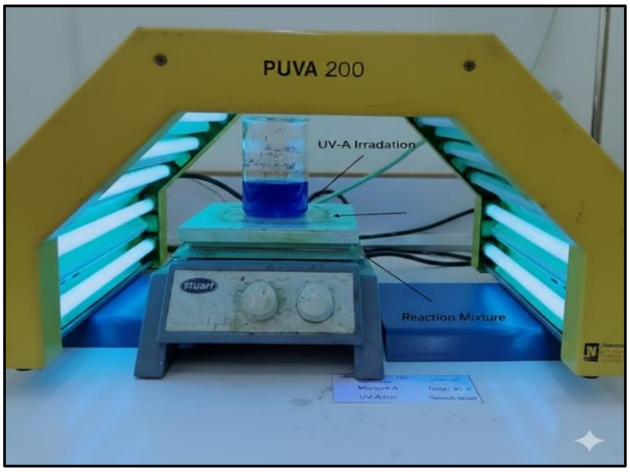

Figure 2. Experimental setup of photocatalysis technology for studying the photodegradation of PAN-PMMA/CeO_2 NCFs

Note: PAN = polyacrylonitrile, PMMA= poly (methyl methacrylate), NCF = nanocomposite fibers

2.6 Evaluation of prepared PAN-PMMA/CeO_2 nanocomposite fibers

To identify the CeO_2 nanoparticle peaks, the samples were subjected to X-ray diffraction at 1.54 Å and 40 kV, with a 2θ range of 20° to 80°. FTIR analysis was performed on the samples at a resolution of 4 cm^{-1} within the spectral range of 500-4000 cm^{-1} to determine the functional groups of the prepared CeO_2 nanoparticles, nanofibers, and NCFs. Subsequently, field emission scanning electron microscopy (FE-SEM) was performed to analyze the morphology of the prepared nanomaterials and fibers. (Tescan, Czech, MIRA III) and Energy-Dispersive X-ray Spectroscopy (EDX), respectively. ImageJ software was used to determine the diameters of CeO_2 nanoparticles and nanofibers. To assess the results of the grafting process and the uniformity of nanoparticle distribution. The optical characteristics were assessed utilising a UV-Vis spectra for the PAN-PMMA mixture and its NCFs incorporating from 2.2 to 6.6 wt.% CeO_2, measured across the range of wavelength 200 to 1100 nm. Finally, the photocatalytic activity of PAN-PMMA/CeO_2 nanofibers with a maximum CeO_2 concentration of 6.6 wt.% was investigated under ultraviolet light to increase the efficiency of the catalytic activity of nanofibers. A higher CeO_2 concentration increases the number of catalytically active sites on the fiber surface, thereby promoting photon absorption and electron-hole pair generation (which initiates photocatalytic reactions).

3. DISCUSSION OF OUTCOMES

3.1 Assessment of X-ray diffraction pattern

In Figure 3, the XRD patterns of the thermally treated CeO_2 nanoparticles are shown. From the diffraction peaks observed at angles 2θ and the diffraction peak levels at 28.55°(111), 33.07°(200), 47.48°(220), 56.34°(311), 59.09°(222), and 69.418°(400), the formation of the CeO_2 nanoparticles with the face-centered cubic (FCC) lattice structure is confirmed [29]. Using the UNITCELL software program, the crystal lattice parameters of CeO_2 were determined to be a = b = c = 5.4113 Å and α = β = γ = 90.000°. The results are consistent with those reported in studies [30] and also with standard results (JCPDS No. 34-0394). Table 2 summarizes crystallographic parameters obtained, including inter-planar distance (d_{hkl}).

Table 2. Crystallographic parameters derived from XRD analysis of CeO_2 nanoparticles

2θ (°)	hkl	FWHM (°)	d_{hkl} (Å, this work)	d_{hkl} (Å, standard)	ε (%)	D (nm)	D (Total Average)
28.55	111	0.79689	3.1237	3.1234	0.00960	10.48	59.38
33.07	200	0.60800	2.7055	2.7056	0.00360	13.64	
47.48	220	0.90667	1.9125	1.9134	0.00047	9.16	
56.34	311	0.67729	1.6310	1.6318	0.00049	12.26	
59.09	222	0.08556	1.5615	1.5622	0.00044	97.15	
69.41	400	0.03778	1.3523	1.3531	0.00059	222.71	

Note: 2θ: diffraction angle; hkl: Miller indices; FWHM: full width at half maximum; dhkl: interplanar spacing (Å); ε: micro-strain; D: crystallite size (nm)

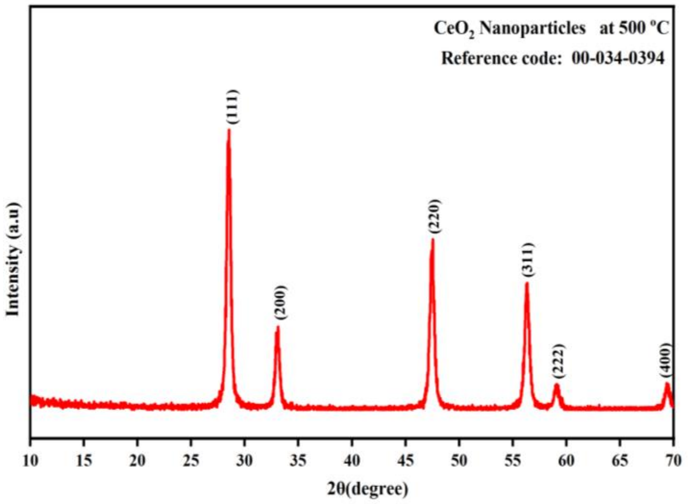

Figure 3. X-ray diffraction (XRD) patterns of CeO_2 nanoparticles

The mean crystallite volume D, microstrain ε, and interplanar spacing (d_{hkl}) were computed using equations [31]:

Bragg's relations

$$2d_{hkl}\sin\theta = \lambda \tag{1}$$

The well-known Scherer's (eq)

$$D = \frac{0.94\lambda}{\beta\cos\theta} \tag{2}$$

and

$$\varepsilon = \frac{\beta\cos\theta}{4} \tag{3}$$

where,

λ: the wavelength (1.54 Å) of CuKα radiation,

β: full width at half maximum (FWHM) of the d_{hkl} diffraction peak,

θ: signifies the Bragg angle of the Miller indices (hkl) peak.

Table 2 contains the values for 2θ, D, ε, d_{hkl}, and FWHM.

3.2 Fourier transform infrared spectroscopy measurements

The FTIR spectra of CeO_2 nanoparticles, PAN-PMMA blend, and its nanocomposites with varying CeO_2 ratios are depicted in Figure 4, which was recorded within the 4000-500 cm^{-1} range. The broadband peak at 3480 cm^{-1} in the FTIR spectrum of CeO_2 is ascribed to the O-H stretching vibration in hydroxyl groups. The bending vibration of C-H stretching is responsible for the absorption peak at 1464 cm^{-1}, while the bands spanning 1500-2000 cm^{-1} are attributed to organic constituents. The Ce-O stretching vibration is represented by the intense band at 741 cm^{-1}. These findings are in accordance with the existing body of research [32]. The asymmetric stretching vibration of CO_2, the bending vibration of CO_2, and the C-O stretching vibration have been assigned to bands at approximately 750 and 1130.28 cm^{-1}, respectively. It is consistent with the study [33]. The PAN-PMMA blend nanofibers with a weight ratio of 85/15 exhibit a wideband peak at 3220 cm^{-1}. This is linked to the stretching vibrations of hydroxyl groups (O-H). Additionally, the peaks at 2945.30 cm^{-1} are specific to polymer chains, while those at 2243.21 cm^{-1} are characteristic of the nitrile group in PAN. The data agree with a previous study [12]. Also, the shape shows analogous intensities across the peaks at 1660.71 cm^{-1} to 538.14 cm^{-1}, resulting from all the ingredients used to prepare the fibers. The results are consistent with a previous study [34].

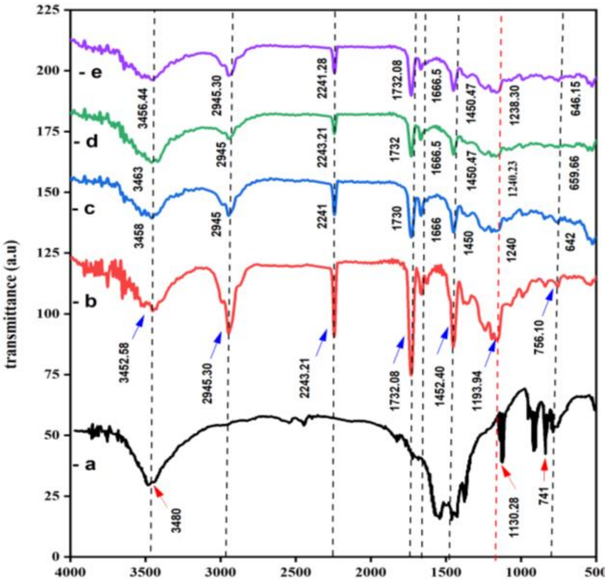

Figure 4. FTIR spectra of (a) CeO$_2$ nanoparticles and PAN-PMMA/CeO$_2$ NCFs containing (b) 0, (c) 2.2, (d) 4.4, (e) 6.6 wt % CeO$_2$

Note: FTIR = Fourier transform infrared spectroscopy, PAN = polyacrylonitrile, PMMA= poly (methyl methacrylate), NCF = nanocomposite fibers

The nanofibers have exhibited a change in functional peak as a result of the CeO$_2$ contribution, as illustrated in Figure 4(c, d, and e). In the samples, powerful bands of PAN and PMMA were observed. at 2945 cm^{-1} (C-H stretching), 2241 cm^{-1} (C ≡ N stretching of PAN), 1730 cm^{-1} (C = O stretching of PMMA), 1666 cm^{-1} (C = C or amide-related vibration), 1240 cm^{-1} (C-O stretching) and 625 cm^{-1} (Ce-O vibration) [35]. In addition, the addition of the nucleating agent PAN-PMMA/CeO$_2$ resulted in a shift in the functional peaks of PAN-PMMA/CeO$_2$ up to 5-10 cm^{-1}, which is the highest ratio in this study. This result was due to the addition of the most functional groups, which increased the peak intensities. The spectrum of PAN-PMMA exhibits substantial alterations and vigorous interfacial engagement as a result of the variation in the CeO$_2$ nanoparticles ratio, as evidenced by the infrared spectra. This result may be attributed to the formation of H$_2$ bonds between the O-H groups in the CeO$_2$ and the C = O groups in the PAN-PMMA.

Additionally, this may be associated with the charge that is transferred to the other atoms that are dissociated from the C = O function group. The absorption was reduced, and the functional summits were displaced to the low-wavenumber region due to the double-bond character of C = O. The results obtained are consistent with previous research that confirmed significant CeO$_2$-polymer interactions by demonstrating analogous shifts in FTIR peaks upon the addition of metal oxide nanoparticles to polymeric matrices [36].

3.3 Morphological analysis

To investigate surface morphology and confirm the elemental composition of CeO$_2$ nanoparticles, the PAN-PMMA mixture, and NCFs, FE-SEM images in conjunction with EDX spectroscopy were employed, as illustrated in Figures 5-8. The morphology of CeO$_2$ nanoparticles is regularly spherical, with some surface roughness, as shown in Figure 5(a). FE-SEM images were captured at 120000× magnification and allow for precise visualization and characterization of each nanoparticle. Quantitative analysis of morphology was carried out by measuring the sizes of 100 randomly selected particles (n = 100). Size measurements of the nanoparticles were performed using ImageJ, a software often used for quantitative SEM imaging. The average diameter of the CeO$_2$ nanoparticles was found to be 81.35 ± 12.48 nm. For further analysis of the size distribution, ImageJ was used, resulting in the histogram shown in Figure 5(b). The obtained histogram shows a Gaussian-like distribution, suggesting a uniform nanoscale size distribution and high nanoparticle homogeneity. The spherical shape of CeO$_2$ nanoparticles can be explained by surface energy minimization, which provides stability, as reported previously [37]. Figure 6 is a depiction of the EDX spectrum and FE-SEM-EDX elemental map of CeO$_2$ nanofibers at pH 9, which have been annealed at 500 °C for 2.5 h. Green indicates the presence of cerium, while purple indicates oxygen in the elemental mapping images. The results indicated no peaks other than those associated with CeO$_2$, consistent with previous findings [38]. The FE-SEM images and diameter distribution profiles of the polymer blend and NCF samples are shown in Figures 7 and 8, respectively. FE-SEM images of the nanofiber samples were recorded at 5000× and 10000× magnification for general morphological observation and diameter calculation, respectively.

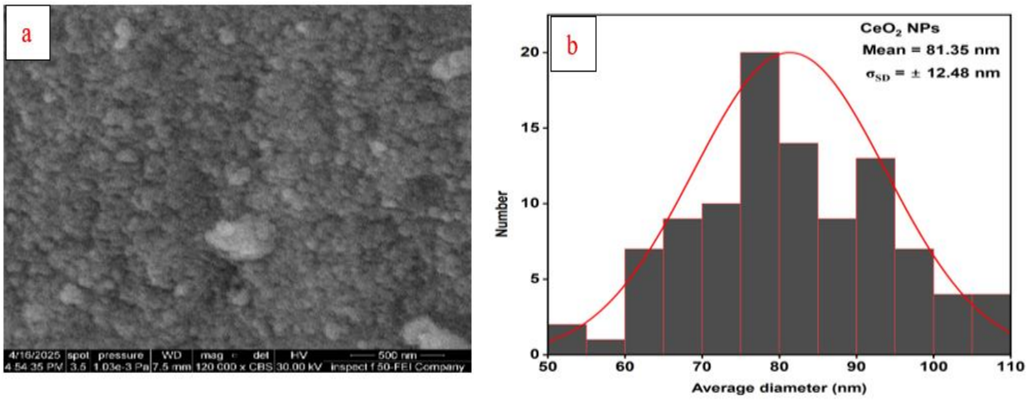

Figure 5. (a) FE-SEM picture and (b) mean diameter with standard dispersion of CeO$_2$ nanoparticles

Note: FE-SEM = field emission scanning electron microscope

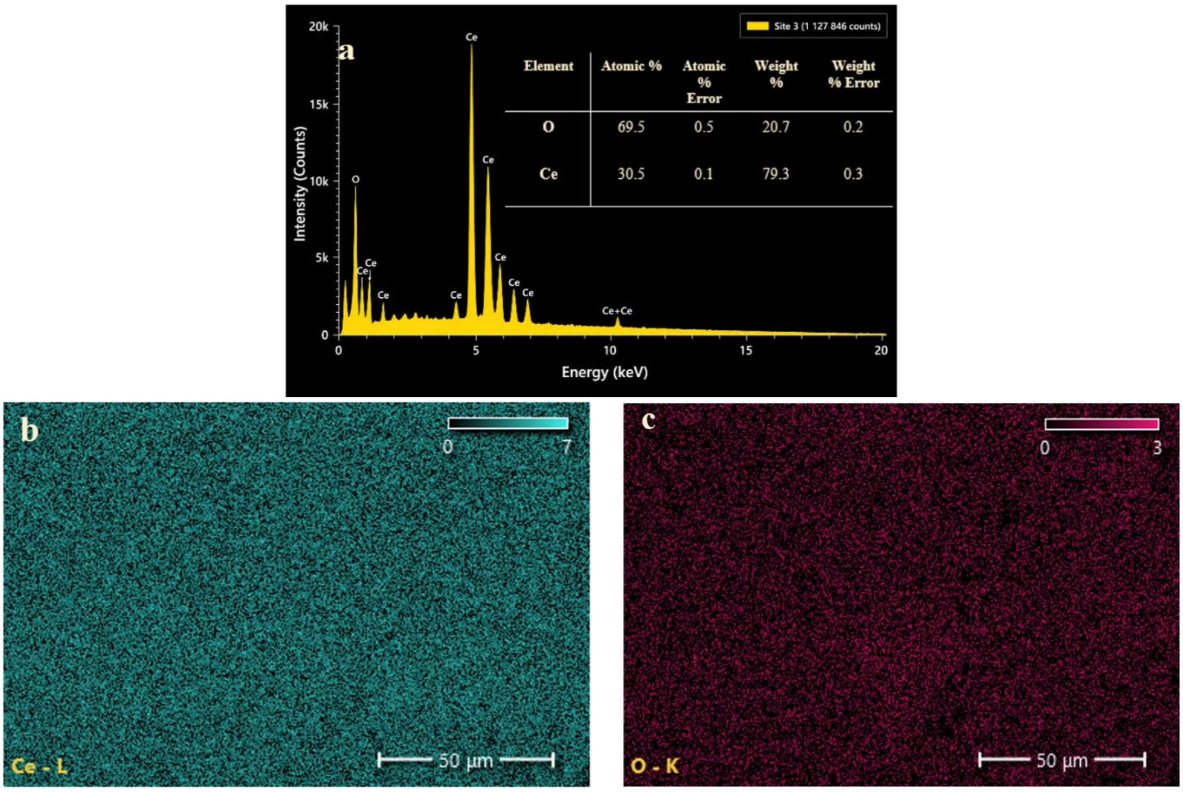

Element	Atomic %	Atomic % Error	Weight %	Weight % Error
O	69.5	0.5	20.7	0.2
Ce	30.5	0.1	79.3	0.3

Figure 6. EDXs and FE-SEM-EDXs mapping spectra of CeO_2 nanoparticles annealed at 500 °C for pH 9
Note: FE-SEM = field emission scanning electron microscope, EDX = energy dispersive X-ray spectroscopy

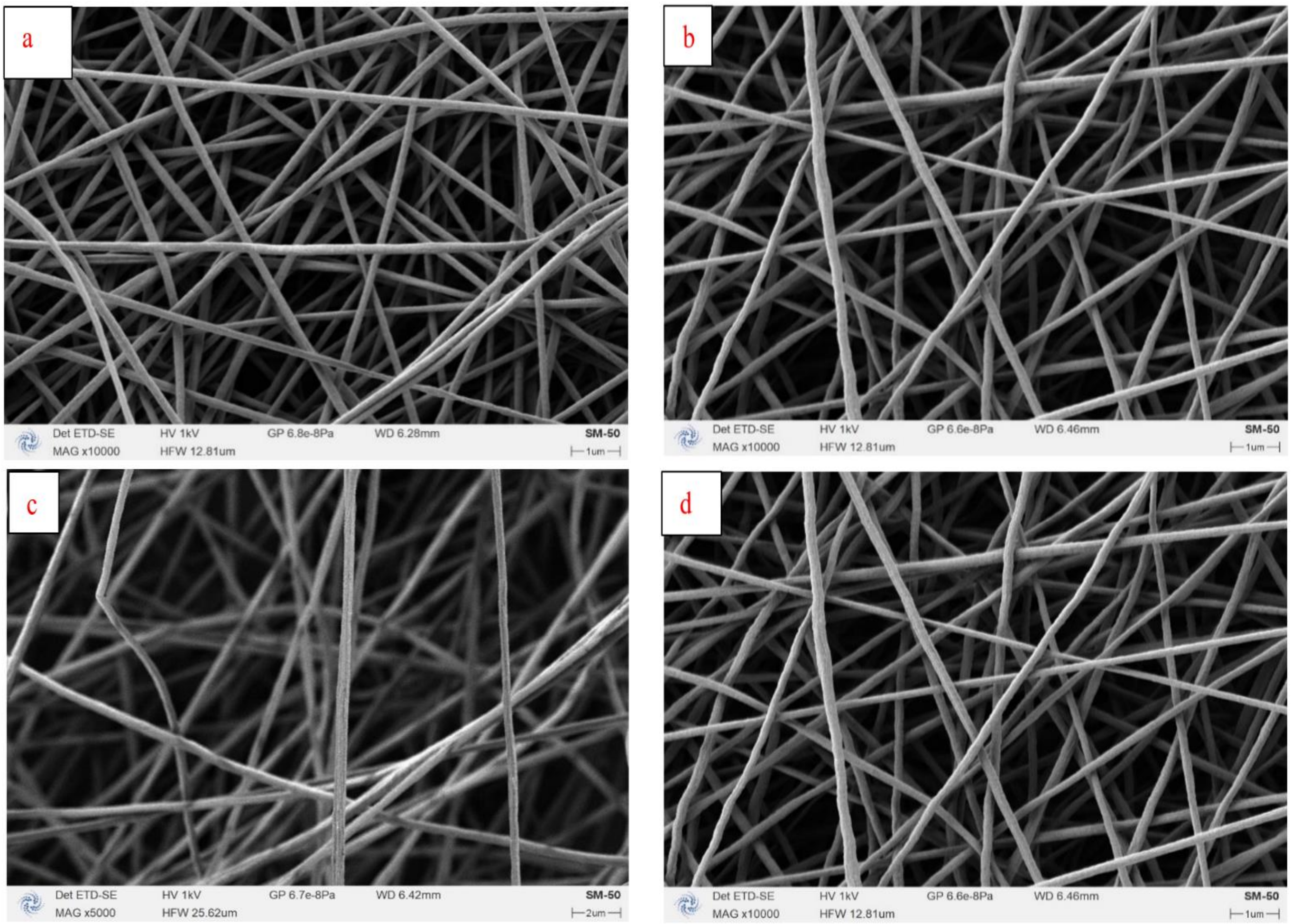

Figure 7. FE-SEM picture of PAN-PMMA blend and its composite nanofibers with 2.2, 4.4, and 6.6 wt.% CeO_2, respectively
Note: FE-SEM = field emission scanning electron microscope, PAN = polyacrylonitrile, PMMA= poly (methyl methacrylate)

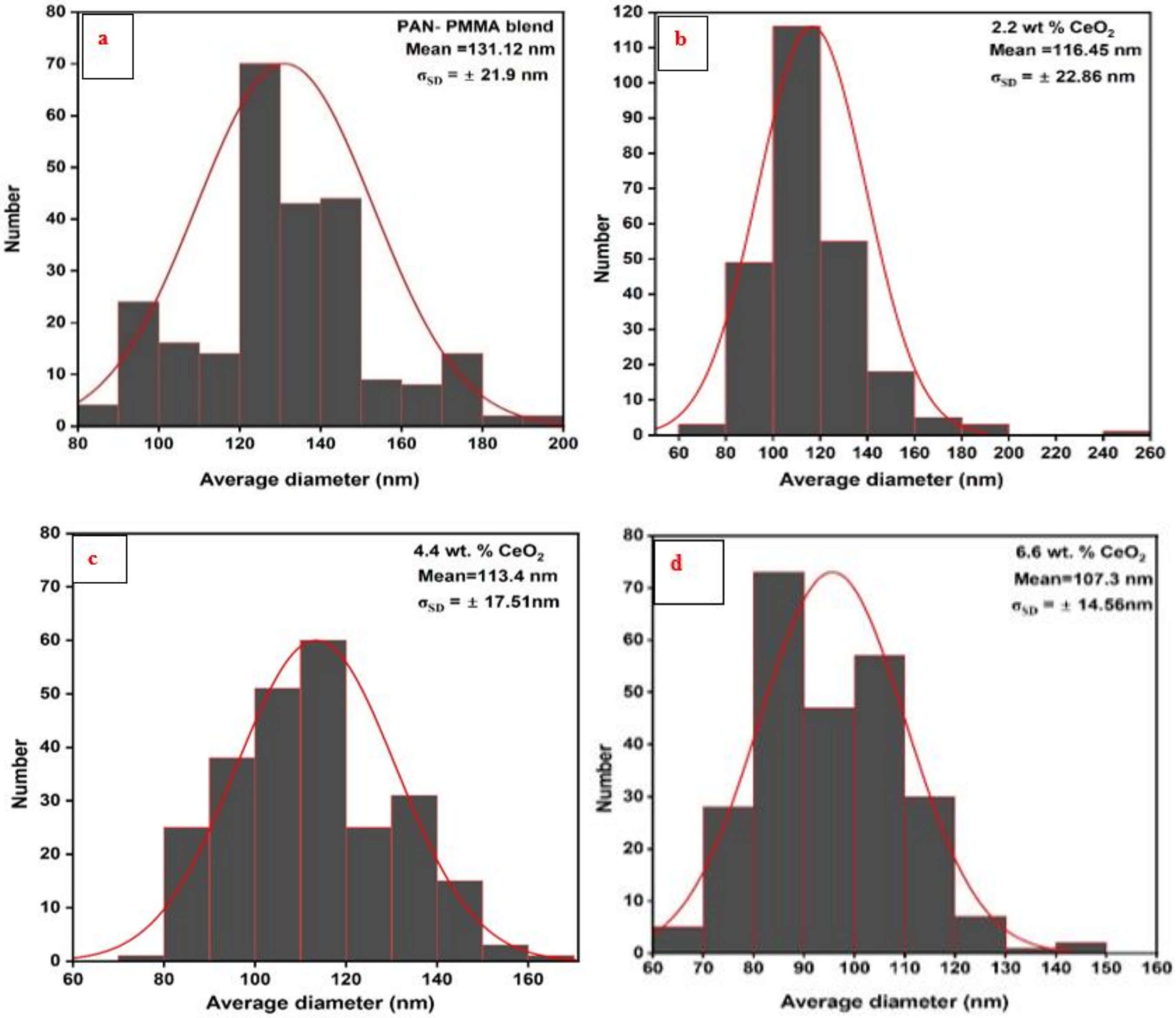

Figure 8. Mean diameter with standard deviation of PAN-PMMA blend and its composite nanofibers containing 2.2, 4.4, and 6.6 wt.% CeO_2, respectively

Note: PAN = polyacrylonitrile, PMMA= poly (methyl methacrylate)

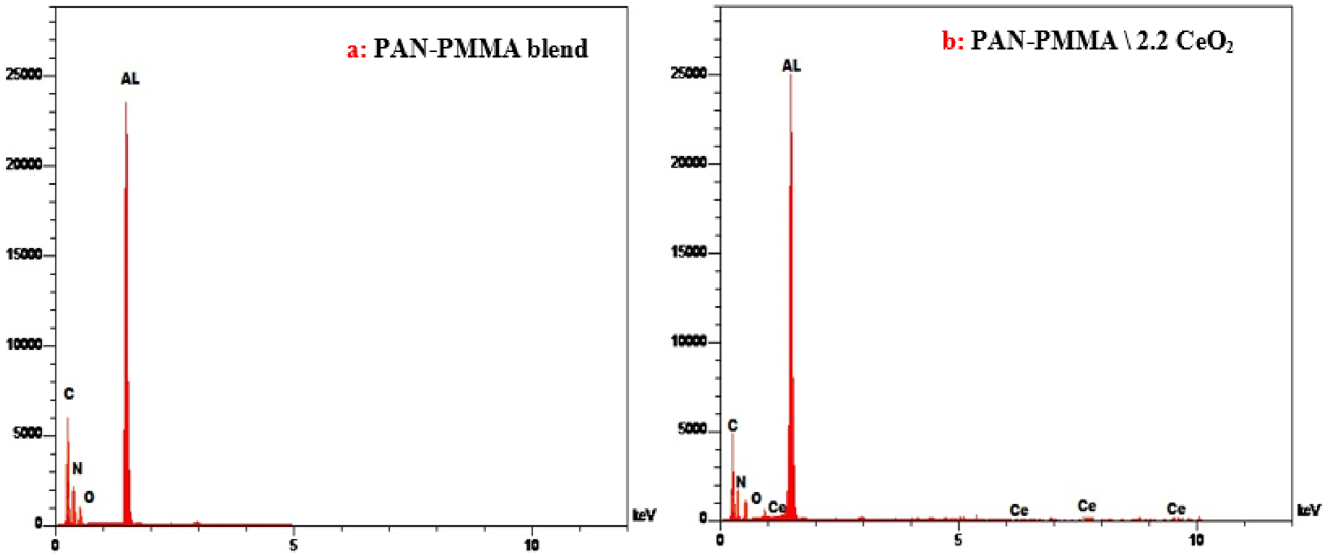

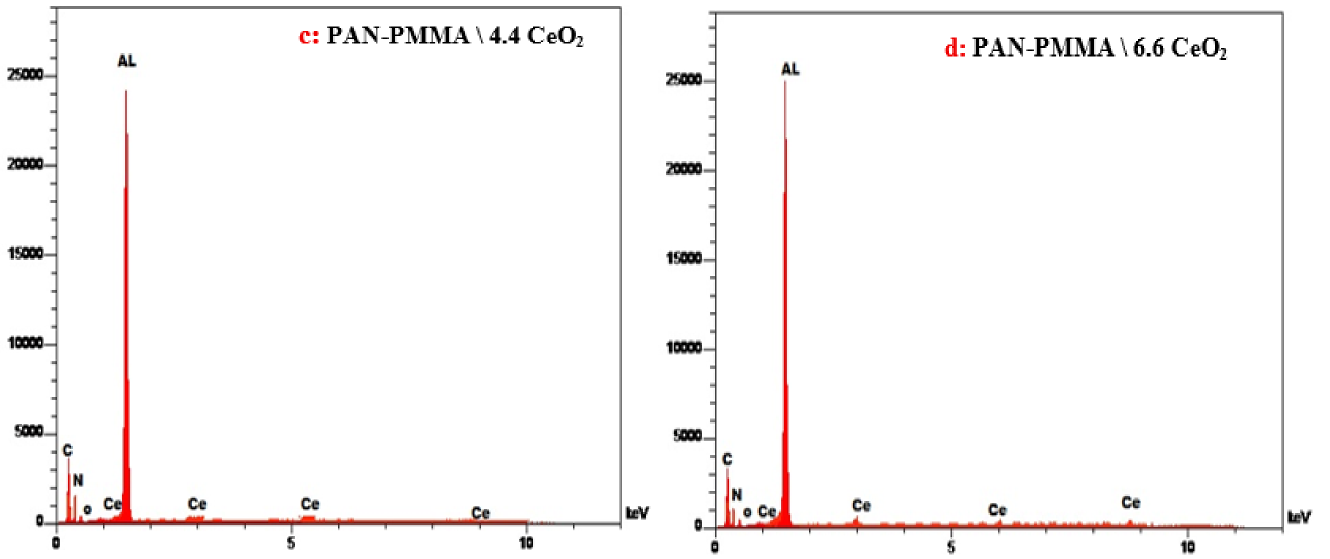

Figure 9. EDX analysis and average fiber diameter (±SD) of PAN-PMMA blend and its nanocomposites fibers with 2.2, 4.4, and 6.6 wt.% CeO_2

Note: EDX= energy dispersive X-ray spectroscopy, PAN = polyacrylonitrile, PMMA= poly (methyl methacrylate)

The diameter of the nanofibers was calculated using ImageJ with a minimum of 100 randomly selected fibers (n = 100). PAN-PMMA nanofibers in Figure 7(a) and Figure 8(a) showed a homogeneous and entangled fibrous structure with an average diameter of around 131 ± 21.9 nm. When 2.2 wt.% CeO_2 was added (Figure 7(b) and Figure 8(b)), the average diameter became 116 ± 22.88 nm, reflecting a reduction in diameter with a rather broad distribution.

Adding a higher content of 4.4 wt.% CeO_2 (Figure 7(c) and Figure 8(c)) resulted in a decrease in diameter to 113 ± 17.51 nm. It is worth noting that, along with diameter reduction, the distribution was narrower in this sample than in the previous samples (confirmed by histograms and box plots generated in ImageJ). Finally, at 6.6 wt.% CeO_2 (Figure 7(d) and Figure 8(d)), the average diameter was 107 ± 14.56 nm, with an improved distribution and lower fiber dispersiveness.

This effect indicates that CeO_2 nanoparticles considerably affect nanofiber morphology. Such behavior may be explained by the increased solution conductivity induced by CeO_2 nanoparticles, which allows for greater stretching of the electrospinning jet and, consequently, a decreased fiber diameter. Apart from that, changes in solution viscosity could have affected the distribution and uniformity of fibers. Such findings correlate with previously published studies [39]. EDX spectroscopy data on the elements present in polymer blend nanofibers and NCFs with 2.2, 4.4, and 6.6 wt.% CeO_2 is presented in Figure 9. The presence of carbon, nitrogen, and oxygen peaks indicates the polymer structures of PAN and PMMA. Cerium peaks are observed in all nanocomposites, and their intensities increase with increasing ceria content. This observation confirms the nanoparticle distribution's homogeneity within the matrix [40]. A gradual increase in the Ce peak intensity with increasing concentration suggests a high-quality synthesis procedure and no nanoparticle aggregation. Aluminum peaks appear due to the aluminum substrate used for electrospinning, which is typical for EDX analysis. However, they have no significance in chemistry.

In summary, the results indicate that CeO_2 is effectively incorporated into PAN-PMMA nanofibers and can be further explored as a promising material for various technological applications. The latter includes the use of nanofibers as efficient photocatalysts due to improved electron conductivity and surface reactivity [41]. This result indicates the suitability of these materials for advanced functional applications, particularly photocatalysis, given the effective role of cerium and oxygen in enhancing the electronic properties and surface reactivity.

3.4 Assessment of optical properties

To prepare the CeO_2 nanoparticles solution for optical measurements, 0.022 g of CeO_2 nanoparticles was combined with 5 ml of deionised water and stirred for 30 minutes, followed by two rounds of sonication for 3 minutes each. The solution was subsequently dripped onto the glass and allowed to dry. Subsequently, the absorption spectrum was recorded using a UV-Vis spectrometer to study the optical absorption characteristics in the range of 300 to 1200 nm as a function of wavelength, as shown in Figure 10(a). The absorption edge data indicate that the maximum absorption occurs at approximately 400 nm, within the UV region, followed by a gradual decrease with increasing wavelength. Figure 10(b) shows the determination of the direct band gap energy of the CeO_2 nanoparticles using Eq. (4), which was found to be 3 electron volts. This result is consistent with previous research [42]. The absorption coefficient of CeO_2 at pH 9 confirms that CeO_2 possesses good optical properties and acts as a highly efficient UV absorber, given that its absorption edge lies within the ultraviolet range (Figure 10(c)). These results are consistent with the literature [43]. Figure 10(d) and (e) illustrate the indirect photoelectric energy gap (Eg) and absorption of a PAN-PMMA mixture and its nanofibers with proportions of (2.2, 4.4, and 6.6 wt.%) CeO_2, 12 micrometers thick on a glass substrate in the wavelength range of 300 to 1200 nm. The absorption spectra of the nanofibers show improved light absorption with the addition of CeO_2 nanoparticles, particularly in the ultraviolet range (300-400 nm). This result is ascribed to the increased density of active centers and the formation of energy levels associated with oxygen defects. The absorption effect extends into the visible spectrum, suggesting an effective reduction in the optical indirect energy gap. The band gap decreases from 3.4 eV to

2.6 eV, as calculated using Eq. (4). This reduction is attributed to the interaction between the nanoparticles and the polymer matrix, where increasing the nanomaterial percentage causes the polymer chains to become less regular and less crystalline, thereby narrowing the band gap. An absorption shift towards the visible spectrum results from an increase in the overlap of electron orbitals between the nanomaterial employed and the polymer matrix at increasing concentrations. As a result, the decrease in the band gap indicates that the composite's morphology, electrical and optical characteristics have improved, making it more appropriate for photocatalysis applications. These results are similar to those of previous studies [44].

$$(\alpha h\upsilon)^{m} = B\,(h\upsilon - E_{g}^{opt}) \qquad (4)$$

where, α signifies the absorption edge coefficient, *h* represents Planck's constant, *hυ* indicates the photon energy, *B* refers to a material-specific constant, and *m* is equal to 2 for a direct transition or 1/2 for an indirect transition.

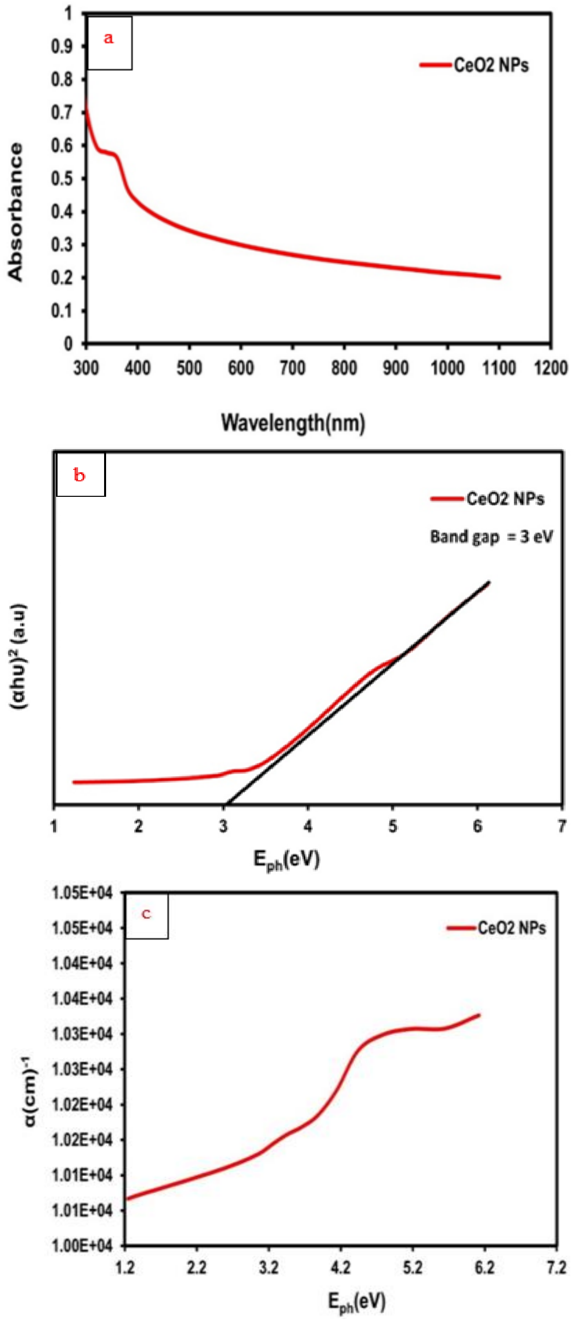

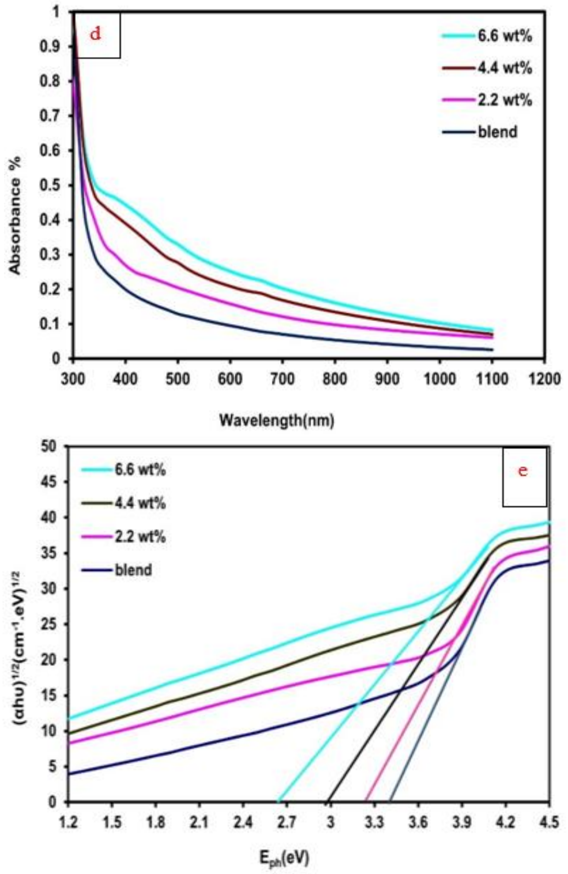

Figure 10. (a, b, and c) Absorbance, and E_g and absorption coefficient of CeO_2 nanoparticles; (d and e) absorbance vs. wavelength and E_g vs. E_{Ph} of PAN-PMMA and PAN-PMMA/CeO_2 NCFs, respectively

Note: PAN = polyacrylonitrile, PMMA = poly (methyl methacrylate), NCF = nanocomposite fibers

3.5 Photodegradation capability

The initial concentration of M.B. used was set at approximately 1.14 mg/L (0.08 mg in 70 mL), with 0.5 g of the fabricated nanofibers used as the photocatalyst. This was determined to ensure a sufficient number of active sites, as well as to maximize interactions between the dye molecules and the nanofibers. The results are consistent with previous literature [45].

Kinetics of photocatalytic destruction of the M.B. solution in the presence of synthesized nanofibers show a definite trend.

The trend can be seen from the rapid decline of absorption within the characteristic wavelength range (~590 nm) in comparison with the control sample (Figure 11). In this case, before exposing the suspension to UV light, the suspension was left in darkness to establish the equilibrium between adsorption and desorption processes. It is important to acknowledge that although photolysis (M.B. + UV) was seen, a dedicated control for the polymer support alone (PAN-PMMA without CeO_2) under UV was not conducted in this investigation. As depicted in Figure 11 and confirmed by data presented in Table 3, the absorbance level was reduced from 0.53 to 0.39 during the initial period. The initial decrease may mostly be ascribed to the dark adsorption of M.B. molecules onto the nanofiber surface. The results are consistent with previous literature [46]. When exposed to UV light, the next steady decrease in the absorbance level was recorded, ranging from 0.39 to 0.11 when the exposure time was extended from

15 to 60 min, leading to an enhancement in the degradation efficiency from 26% to 80%, respectively. It is suggested that the subsequent drop in the absorbance level is associated with the process of photocatalytic degradation, which prevails after achieving equilibrium in the adsorption process, implying that there was a gradual contribution of the photocatalytic reaction to the process. This may occur as a result of electron-hole generation on the CeO_2 surfaces when exposed to the UV light. Oxygen vacancy is another factor that might facilitate the formation of reactive oxygen species such as $O_2^{\bullet -}$ and $^{\bullet}OH$ radicals [47]. Figure 12 depicts the possible mechanism of the oxidation-reduction process in the photodegradation process. From Eq. (5), it can be observed that there was an increase in the efficiency of degradation from 26.48% at 15 minutes to 80% at 60 minutes (see Table 3 and Figure 13). It can be seen that there is a time-dependent process in the process of degradation. Experimental results suggest that the addition of CeO_2 in the PAN-PMMA mixture could potentially contribute to improving adsorption and transferring charges. This is consistent with other findings [48]. The value of the rate constant (k) was determined by obtaining the slope of the linear fit of $\ln(A_0/A)$ versus the irradiation time. Figure 14 shows the corresponding linear plot, yielding a rate constant of 0.0253 min^{-1} with an R^2 of 0.99.

The degrading efficiency values of M.B. were obtained using the following formula [49].

$$Degradation = \frac{A_0 - A_t}{A_0} \times 100\% \qquad (5)$$

where, A_0 is the starting concentration of M.B. dye (before the reaction begins) and A_t is the concentration of M.B. dye after a certain time has passed since the reaction.

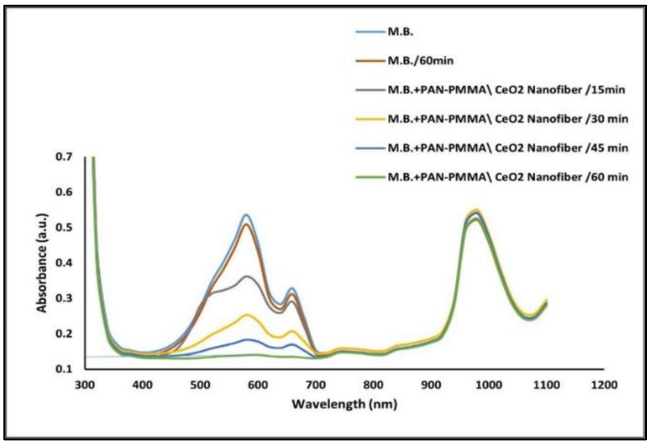

Figure 11. Time-dependent photodegradation$_s$ of M.B. over PAN-PMMA/CeO_2 nanofiber monitored by UV-V is spectroscopy

Note: PAN = polyacrylonitrile, PMMA = poly (methyl methacrylate), M.B. = methylene blue, UV-Vis = ultraviolet-visible

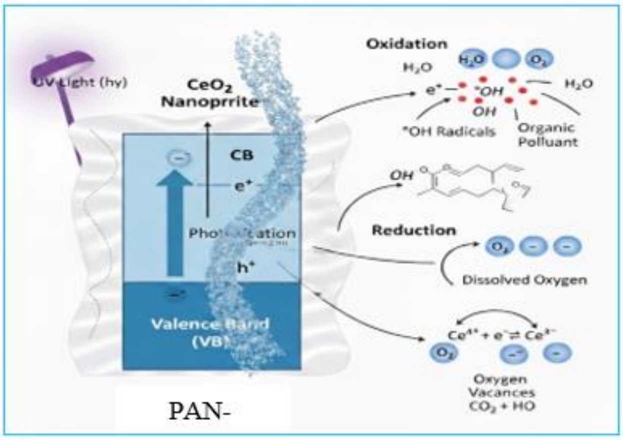

Figure 12. Proposed mechanism of photodegradation of M.B. over PAN-PMMA/CeO_2 nanofibers

Note: PAN = polyacrylonitrile, PMMA = poly (methyl methacrylate), M.B. = methylene blue

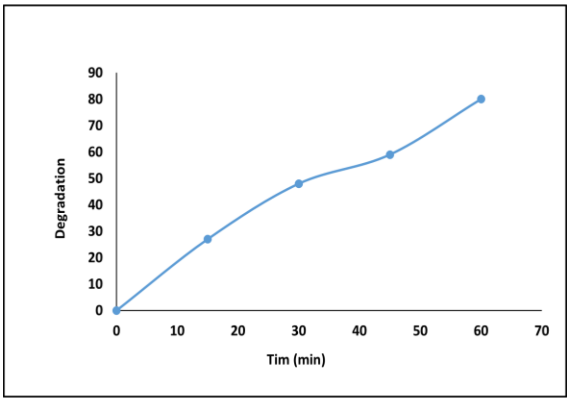

Figure 13. Degradation efficiency curve (%) as a function of time

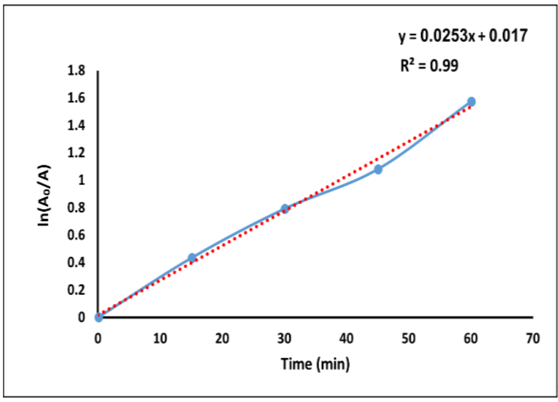

Figure 14. Pseudo-first-order kinetic plot of $\ln(A_0/A)$ versus irradiation time for M.B. degradation over PAN-PMMA/CeO_2 nanofibers

Note: M.B. = methylene blue, PAN = polyacrylonitrile, PMMA = poly (methyl methacrylate)

Table 3. Time-dependent absorbance and degradation efficiency of methylene blue (M.B.) using PAN PMMA/CeO_2 nanofibers under UV irradiation

Sample	Absorbance A_t (a.u.)	Degradation %	A_0/A	$\ln(A_0/A)$
M.B. (A_0, initial)	0.53	0%	1	0
M.B. (UV only, 60 min)	0.51	3%	1.039	0.038

PAN-PMMA/CeO_2 (dark, 60 min)	0.39	26%	1.358	0.306
PAN-PMMA/CeO_2 (UV, 15 min)	0.34	36%	1.559	0.433
PAN-PMMA/CeO_2 (UV, 30 min)	0.24	55%	2.208	0.792
PAN-PMMA/CeO_2 (UV, 45 min)	0.18	67%	2.944	1.080
PAN-PMMA/CeO_2 (UV, 60 min)	0.11	80%	4.818	1.573

4. CONCLUSION

In this work, CeO_2 nanoparticles at pH 9 with an average particle diameter of 81.35 ± 12.48 nm were efficiently synthesized by the hydrothermal technique, as evaluated using ImageJ (100 measurements). PAN-PMMA/CeO_2 nanocomposite fibers with different proportions of CeO_2 nanoparticles were then synthesized by electrospinning fibers for photocatalytic degradation of natural dyes, such as M.B., under UV irradiation. The formation of natural CeO_2 with a cubic FCC crystal shape was demonstrated through XRD structural characterization and FTIR measurements, as well as the interaction between PAN, PMMA, and CeO_2 nanoparticles. detected. FE-SEM snapshots confirmed the uniform interconnected fiber community and EDX analysis confirmed the successful integration and uniform distribution of CeO_2 within the nanofibrous matrix. The optical band gap decreased from 3.4 eV to 2.6 eV with increasing CeO_2 content, indicating improved optical absorption performance. The average fiber diameter decreased with the increase in CeO_2 concentration, due to increased solution conductivity and fiber elongation during electrospinning. Photocatalytic studies showed efficient degradation of M.B., with approximately 80% removal achieved in 60 min under UV irradiation. Over time, the degradation process progressed in a stepwise manner, revealing a time-structured pattern. Furthermore, the kinetic evaluation also suggested that a decay was introduced into the pseudo-first-order kinetic model, with a rate constant (k) of 0.0253 min^{-1} and a high correlation coefficient ($R^2 = 0.99$), indicating a very good fit of the kinetic model. Maybe the more favorable photocatalytic performance is due to better value separation, reduced electron-hole recombination, presence of oxygen vacancies, and Ce^{3+}/Ce^{4+} redox cycling. These compounds result in dye degradation.

REFERENCES

[1] Trandafilović, L.V., Jovanović, D.J., Zhang, X., Ptasińska, S., Dramićanin, M.D. (2017). Enhanced photocatalytic degradation of methylene blue and methyl orange by ZnO:Eu nanoparticles. Applied Catalysis B: Environmental, 203: 740-752. https://doi.org/10.1016/j.apcatb.2016.10.063

[2] Suganthi, S., Vignesh, S., Raj, V., Manoharadas, S., Pandiaraj, S., Kim, H. (2023). Synergistic influence of vanadium pentoxide-coupled graphitic carbon nitride composite for photocatalytic degradation of organic pollutant: Stability and involved Z-scheme mechanism. Environmental Research, 231(3): 116288. https://doi.org/10.1016/j.envres.2023.116288

[3] Intarasuwan, K., Amornpitoksuk, P., Suwanboon, S., Graidist, P. (2017). Photocatalytic dye degradation by ZnO nanoparticles prepared from X2C2O4 (X = H, Na and NH4) and the cytotoxicity of the treated dye solutions. Separation and Purification Technology, 177: 304-312. https://doi.org/10.1016/j.seppur.2016.12.040

[4] Zhang, A.Y., Wang, W.K., Pei, D.N., Yu, H.Q. (2016). Degradation of refractory pollutants under solar light irradiation by a robust and self-protected ZnO/CdS/TiO2 hybrid photocatalyst. Water Research, 92: 78-86. https://doi.org/10.1016/j.watres.2016.01.045

[5] Liu, X., Jin, A., Jia, Y., Xia, T., Deng, C., Zhu, M., Chen, X. (2017). Synergy of adsorption and visible-light photocatalytic degradation of methylene blue by a bifunctional Z-scheme heterojunction of WO3/g-C3N4. Applied Surface Science, 405: 359-371. https://doi.org/10.1016/j.apsusc.2017.02.025

[6] Chang, K.L., Sun, Q., Peng, Y.P., Lai, S.W., Sung, M., Huang, C.Y., Lin, Y.C. (2016). Cu2O loaded titanate nanotube arrays for simultaneously photoelectrochemical ibuprofen oxidation and hydrogen generation. Chemosphere, 150: 605-614. https://doi.org/10.1016/j.chemosphere.2016.02.016

[7] Munoz-Batista, M.J., Fernández-García, M., Kubacka, A. (2015). Promotion of CeO2-TiO2 photoactivity by g-C3N4: ultraviolet and visible light elimination of toluene. Applied Catalysis B: Environmental, 164: 261-270. https://doi.org/10.1016/j.apcatb.2014.09.037

[8] Huda, A., Suman, P.H., Torquato, L.D.M., Silva, B.F., Handoko, C.T., Gulo, F., Orlandi, M.O. (2019). Visible light-driven photoelectrocatalytic degradation of acid yellow 17 using Sn3O4 flower-like thin films supported on Ti substrate (Sn3O4/TiO2/Ti). Journal of Photochemistry and Photobiology A: Chemistry, 376: 196-205. https://doi.org/10.1016/j.jphotochem.2019.01.039

[9] Wang, X., Wu, Q., Ma, H., Ma, C., Yu, Z., Fu, Y., Dong, X. (2019). Fabrication of PbO2 tipped Co3O4 nanowires for efficient photoelectrochemical decolorization of dye (reactive brilliant blue KN-R) wastewater. Solar Energy Materials and Solar Cells, 191: 381-388. https://doi.org/10.1016/j.solmat.2018.12.005

[10] Fernández-Domene, R.M., Roselló-Márquez, G., Sánchez-Tovar, R., Lucas-Granados, B., Garcia-Anton, J. (2019). Photoelectrochemical removal of chlorfenvinphos by using WO3 nanorods: Influence of annealing temperature and operation pH. Separation and Purification Technology, 212: 458-464. https://doi.org/10.1016/j.seppur.2018.11.049

[11] Mousavi, M.R., Rafizadeh, M., Sharif, F. (2016). Effect of electrospinning on the ionic conductivity of polyacrylonitrile/polymethyl methacrylate nanofibrous membranes: Optimization based on the response surface method. Iranian Polymer Journal (English Edition), 25(6): 525-537. https://doi.org/10.1007/s13726-016-0444-6

[12] Kaerkitcha, N., Chuangchote, S., Sagawa, T. (2016). Control of physical properties of carbon nanofibers obtained from coaxial electrospinning of PMMA and PAN with adjustable inner/outer nozzle-ends. Nanoscale Research Letters, 11(1): 17-21. https://doi.org/10.1186/s11671-016-1416-7

[13] Kim, C., Jeong, Y.I., Ngoc, B.T.N., Yang, K.S., Kojima, M., Kim, Y.A., Lee, J.W. (2007). Synthesis and characterization of porous carbon nanofibers with hollow

cores through the thermal treatment of electrospun copolymeric nanofiber webs. Small, 3(1): 91-95. https://doi.org/10.1002/smll.200600243

[14] Mousavi, M.R., Rafizadeh, M., Sharif, F. (2015). Investigation of effect of electrospinning parameters on the morphology of Polyacrylonitrile/Polymethylmethacrylate Nanofibers: A Box-Behnken-based study. Journal of Macromolecular Science Part B, 54(8): 975-991. https://doi.org/10.1080/00222348.2015.1042628

[15] Prasanth, R., Aravindan, V., Srinivasan, M. (2012). Novel polymer electrolyte based on cob-web electrospun multi component polymer blend of polyacrylonitrile/poly (methyl methacrylate)/polystyrene for lithium ion batteries-Preparation and electrochemical characterization. Journal of Power Sources, 202: 299-307. https://doi.org/10.1016/j.jpowsour.2011.11.057

[16] Akashi, H., Sekai, K., Tanaka, K.I. (1998). A novel fire-retardant polyacrylonitrile-based gel electrolyte for lithium batteries. Electrochimica Acta, 43(10-11): 1193-1197. https://doi.org/10.1016/S0013-4686(97)10019-6

[17] Jung, H.R., Lee, W.J. (2011). Electrochemical characteristics of electrospun poly (methyl methacrylate)/polyvinyl chloride as gel polymer electrolytes for lithium ion battery. Electrochimica Acta, 58: 674-680.

[18] Abdullah, S.S., Kadhim, M.A., Al-Bermany, E. (2021). Graphene-reinforced the structure and mechanical properties of new PMMA-PVA hybrid nanocomposites. IOP Conference Series: Materials Science and Engineering, 1094(1): 012138. https://doi.org/10.1088/1757-899x/1094/1/012138

[19] Mpukuta, O.M., Dincer, K., Erdal, M.O. (2019). Investigation of electrical conductivity of PAN nanofibers containing silica nanoparticles produced by electrospinning method. Materials Today: Proceedings, 18(Part 5): 1927-1935. https://doi.org/10.1016/j.matpr.2019.06.683

[20] Choi, S.Y., Han, E.M., Park, K.H. (2019). Porosity control of electrospun PAN/PMMA nanofiber webs. Molecular Crystals and Liquid Crystals, 688(1): 68-74. https://doi.org/10.1080/15421406.2019.1651070

[21] Kusmierek, E. (2020). A CeO2 semiconductor as a photocatalytic and photoelectrocatalytic material for the remediation of pollutants in industrial wastewater: A review. Catalysts, 10(12): 1435. https://doi.org/10.3390/catal10121435

[22] Huang, K., Li, Y.H., Lin, S., Liang, C., Xu, X., Zhou, Y.F., Lei, M. (2014). One-step synthesis of reduced graphene oxide-CeO2 nanocubes composites with enhanced photocatalytic activity. Materials Letters, 124: 223-226. https://doi.org/10.1016/j.matlet.2014.03.023

[23] Yin, D., Zhao, F., Zhang, L., Zhang, X., Liu, Y., Zhang, T., Chen, Z. (2016). Greatly enhanced photocatalytic activity of semiconductor CeO2 by integrating with upconversion nanocrystals and graphene. RSC Advances, 6(105): 103795-103802. https://doi.org/10.1039/C6RA19219J

[24] Wang, B., Zhu, B., Yun, S., Zhang, W., Xia, C., Afzal, M., Wang, H. (2019). Fast ionic conduction in semiconductor CeO2-δ electrolyte fuel cells. NPG Asia Materials, 11(1): 51. https://doi.org/10.1038/s41427-019-0152-8

[25] Aboutaleb, W.A., El-Salamony, R.A. (2019). Effect of Fe2O3-CeO2 nanocomposite synthesis method on the Congo red dye photodegradation under visible light irradiation. Materials Chemistry and Physics, 236: 121724. https://doi.org/10.1016/j.matchemphys.2019.121724

[26] Phyu, M.P., Inkiaesai, N., Tasit, W., Yanshai, P., Sae-Long, W., Arun, S., Limkatanyu, S. (2026). Limit load of cellular beams governed by web-post bending failure in integrated structural systems. Journal of Complex and Multiphysics Engineering Systems, 1(1): 110-121. https://doi.org/10.56578/jcmes010107

[27] Ramezanzadeh, B., Bahlakeh, G., Ramezanzadeh, M. (2018). Polyaniline-cerium oxide (PAni-CeO2) coated graphene oxide for enhancement of epoxy coating corrosion protection performance on mild steel. Corrosion Science, 137: 111-126. https://doi.org/10.1016/j.corsci.2018.03.038

[28] Sharma, R.P., Barik, B.K., Praharaj, S., Kumar, V.V., Sharma, A. (2026). Hall-effect-modulated thermal transport enhancement in hybrid nanofluid flow over a stretching surface using Taguchi optimization. Journal of Complex and Multiphysics Engineering Systems, 1(1): 82-97. https://doi.org/10.56578/jcmes010105

[29] Huang, Y.C., Wu, S.H., Hsiao, C.H., Lee, A.T., Huang, M.H. (2020). Mild synthesis of size-tunable CeO_2 octahedra for band gap variation. Chemistry of Materials, 32(6), 2631-2638. https://doi.org/10.1021/acs.chemmater.0c00318

[30] Calvache-Muñoz, J., Prado, F.A., Rodríguez-Páez, J.E. (2017). Cerium oxide nanoparticles: Synthesis, characterization and tentative mechanism of particle formation. Colloids and Surfaces A: Physicochemical and Engineering Aspects, 529: 146-159. https://doi.org/10.1016/j.colsurfa.2017.05.059

[31] Willardson, R.K., Beer, A.C. (1977). Semiconductors and Semimetals. New York: Academic Press.

[32] Farahmandjou, M., Zarinkamar, M., Firoozabadi, T.P. (2016). Synthesis of Cerium Oxide (CeO2) nanoparticles using simple CO-precipitation method. Revista Mexicana de Física, 62(5): 496-499.

[33] Ravishankar, T.N., Ramakrishnappa, T., Nagaraju, G., Rajanaika, H. (2015). Synthesis and characterization of CeO2 nanoparticles via solution combustion method for photocatalytic and antibacterial activity studies. ChemistryOpen, 4(2): 146-154. https://doi.org/10.1002/open.201402046

[34] Khan, W.S., Asmatulu, R., Rodriguez, V., Ceylan, M. (2014). Enhancing thermal and ionic conductivities of electrospun PAN and PMMA nanofibers by graphene nanoflake additions for battery-separator applications. International Journal of Energy Research, 38(15): 2044-2051. https://doi.org/10.1002/er.3188

[35] Mohammed, Y.A.Y.A., Ma, F., Liu, L., Zhang, C., Dong, H., Wang, Q., Al-Wahbi, A.A. (2021). Preparation of electrospun polyvinylidene fluoride/amidoximized polyacrylonitrile nanofibers for trace metal ions removal from contaminated water. Journal of Porous Materials, 28(2): 383-392. https://doi.org/10.1007/s10934-020-00995-w

[36] Ahamed, M., Mansoor, S., Lateef, R., Luiz, G., Alhadlaq, H.A. (2025). Oxygen-vacancy engineering and junction design in CeO2 nanomaterials for photocatalysis and antibacterial action: A review. Results in Engineering, 28: 108076. https://doi.org/10.1016/j.rineng.2025.108076

[37] Jayakumar, G., Irudayaraj, A.A., Raj, A.D. (2017). Particle size effect on the properties of cerium oxide (CeO2) nanoparticles synthesized by hydrothermal method. Mechanics, Materials Science & Engineering Journal, 9(1): 1-6. https://doi.org/10.2412/mmse.3.4.481

[38] Khan, M.A., Siddique, M.A.R., Sajid, M., Karim, S., Ali, M.U., Abid, R., Bokhari, S.A.I. (2023). A comparative study of green and chemical cerium oxide nanoparticles (CeO2-NPs): From synthesis, characterization, and electrochemical analysis to multifaceted biomedical applications. BioNanoScience, 13(2): 667-685. https://doi.org/10.1007/s12668-023-01114-0

[39] Abdelamir, A.I., Hashim, F.S. (2025). Solvothermal synthesis of CZTS nano-structure based-electrospun PAN nanofibers impact on characterizations and antibacterial activity. Nano-Structures & Nano-Objects, 43: 101517. https://doi.org/10.1016/j.nanoso.2025.101517

[40] Ramakrishna, S., Fujihara, K., Teo, W.E., Lim, T.C., Ma, Z. (2005). An Introduction to Electrospinning and Nanofibers. Singapore: World Scientific. https://doi.org/10.1142/5894

[41] Goldstein, J.I., Newbury, D.E., Michael, J.R., Ritchie, N.W.M., Scott, J.H.J., Joy, D.C. (2018). Scanning Electron Microscopy and X-Ray Microanalysis. Springer.

[42] Chibac-Scutaru, A.L., Podasca, V., Dascalu, I.A., Melinte, V. (2022). Exploring the influence of synthesis parameters on the optical properties for various CeO2 NPs. Nanomaterials, 12(9): 1-15. https://doi.org/10.3390/nano12091402

[43] Aziz, S.B., Dannoun, E.M., Tahir, D.A., Hussen, S.A., Abdulwahid, R.T., Nofal, M.M., Brevik, I. (2021). Synthesis of PVA/CeO2 based nanocomposites with tuned refractive index and reduced absorption edge: Structural and optical studies. Materials, 14(6): 1570. https://doi.org/10.3390/ma14061570

[44] Khudher, R.H., Hasan, A.A. (2022). Effect of lithium salts on the optical properties of poly acrylonitrile/poly methyl methacrylate blends. Chemical Methodology, 6: 872-885. https://doi.org/10.22034/chemm.2022.354600.1587

[45] Ao, Z.F., Qiao, Z.L., Shen, Z.G., Liu, T., He, W.X., Liu, X.W., Teng, Z.X., Yang, H.Y., Wang, J.X., Cao, D.P. (2025). Constructing frustrated Lewis pairs on defect-engineered biphasic catalysts for polyester depolymerization. Applied Catalysis B : Environment and Energy, 380: 125763. https://doi.org/10.1016/j.apcatb.2025.12576

[46] Ahmed, G., Hanif, M., Zhao, L., Hussain, M., Khan, J., Liu, Z. (2016). Defect engineering of ZnO nanoparticles by graphene oxide leading to enhanced visible light photocatalysis. Journal of Molecular Catalysis A: Chemical, 425: 310-321. https://doi.org/10.1016/j.molcata.2016.10.026

[47] Ajam, A.M., Abass, K.H. (2026). Structural and optical engineering of Bi2O3 nanostructures for enhanced visible-light photocatalysis. Catalysis Letters, 156(2): 41. https://doi.org/10.1007/s10562-025-05262-8

[48] Melinte, V., Stroea, L., Chibac-scutaru, A.L. (2019). Polymer nanocomposites for photocatalytic applications. Catalysts, 9(12): 986. https://doi.org/10.3390/catal9120986

[49] Sh, F., Alkaim, A.F., Mahdi, S.M., Omran, A.H. (2019). Photocatalytic degradation of GRL dye from aqueous solutions in the presence of ZnO / Fe2O3 nanocomposites. Composites Communications, 16: 111-116. https://doi.org/10.1016/j.coco.2019.09.008

NOMENCLATURE

PAN	Polyacrylonitrile
PMMA	Poly (methyl methacrylate)
S_0	PAN-PMMA blend
S_1	PAN-PMMA 2.2 wt.% CeO_2
S_2	PAN-PMMA 4.4 wt.% CeO_2
S_3	PAN-PMMA 6.6 wt.% CeO_2
NCFs	Nanocomposite fiber
CeO_2	cerium dioxide
XRD	X-ray diffraction
EDX	Energy dispersive X-ray spectroscopy
FTIR	Fourier transform infrared spectroscopy
FE-SEM	Field emission scanning electron microscope
M.B.	Methylene blue
UV	Ultraviolet
E_{ph}	Photon energy
E_g	Energy gap